Current Methods in the Automatic Tissue Segmentation of 3D Magnetic Resonance Brain Images

Alan Wee-Chung Liew[1] and Hong Yan[2,3]

[1]*Department of Computer Science and Engineering, The Chinese University of Hong Kong, Shatin, Hong Kong,* [2]*Department of Computer Engineering and Information Technology, City University of Hong Kong, Kowloon Tong, Hong Kong,* [3]*School of Electrical and Information Engineering, University of Sydney, NSW 2006, Australia*

Abstract: Accurate segmentation of magnetic resonance (MR) images of the brain is of interest in the study of many brain disorders. In this paper, we provide a review of some of the current approaches in the tissue segmentation of MR brain images. We broadly divided current MR brain image segmentation algorithms into three categories: classification-based, region-based, and contour-based, and discuss the advantages and disadvantages of these approaches. We also briefly review our recent work in this area. We show that by incorporating two key ideas into the conventional fuzzy c-means clustering algorithm, we are able to take into account the local spatial context and compensate for the intensity nonuniformity (INU) artifact during the clustering process. We conclude this review by pointing to some possible future directions in this area.

Keywords: Medical imaging, magnetic resonance imaging, brain tissue segmentation, intensity nonuniformity artifact, partial volume artifact, fuzzy clustering, image segmentation.

1. INTRODUCTION

Magnetic resonance imaging (MRI) provides rich three-dimensional (3D) information about the human soft tissue anatomy [1]. It reveals fine details of anatomy, and yet is noninvasive and does not require ionizing radiation such as x-rays. It is a highly flexible technique where contrast between one tissue and another in an image can be varied simply by varying the way the image is made. For example, by altering radio-frequency (RF) and gradient pulses, and by carefully choosing relaxation timings, it is possible to highlight different components in the object being imaged and produce high contrast images. The rich anatomy information provided by MRI has made it an indispensable tool for medical diagnosis in recent years

Applications that use the morphologic contents of MRI frequently require segmentation of the image volume into tissue types. For example, accurate segmentation of MR images of the brain is of interest in the study of many brain disorders. In multiple sclerosis, quantification of white matter lesions is necessary for drug treatment assessment [2]. In schizophrenia, epilepsy or Alzheimer's disease, volumetric analysis of gray matter (GM), white matter (WM) and cerebrospinal fluid (CSF) is important to characterize morphological differences between subjects [3, 4, 5-8]. Such studies typically involve vast amount of data. Currently, in many clinical studies segmentation is still mainly manual or strongly supervised by a human expert. The level of operator supervision impacts the performance of the segmentation method in terms of time consumption, leading to infeasible procedures for large datasets. Manual segmentation also shows large intra- and inter-observer variability, making the segmentation irreproducible and deteriorating the precision of the analysis of the segmentation. Hence, there is a real need for automated MRI segmentation tools.

The automatic segmentation of MR images has been an area of intense study [9, 10]. However, this task has proven problematic, due to the many artifacts in the imaging process. In this paper, we review some of the current approaches in the tissue segmentation of MR brain images. We provide a mathematical formulation of the MRI segmentation problem, and an overview of various MRI segmentation methods, which we have broadly divided into three categories: classification-based, region-based, and contour-based. Then, we provide a discussion of our own work in this area, and provide some experimental results indicating the superior performance of our approach. We conclude this review by pointing out some possible future directions.

2. MAGNETIC RESONANCE IMAGING

Magnetic resonance imaging is an imaging technique used primarily in medical settings to produce high quality images of the inside of the human body. In MRI, the image is a map of the local transverse magnetization of the hydrogen nuclei. This transverse magnetization in turn depends on several intrinsic properties of the tissue. In this section, we give a brief description of the principles of MR imaging, the readers are referred to [11, 12] for further details. MRI is based on the principles of nuclear magnetic resonance (NMR). The NMR phenomenon relies on the fundamental property that protons and neutrons that make up a nucleus possess an intrinsic angular momentum called spin. When protons and neutrons combine to form nucleus, they combine with oppositely oriented spins. Thus, nuclei with an even number of protons and neutrons have no net spin, whereas nuclei with an odd number of protons or neutrons possess a net spin. Hydrogen nuclei have an NMR signal since its nucleus is made up of only a single proton

*Address correspondence to this author at the Department of Computer Science and Engineering, The Chinese University of Hong Kong, Shatin, Hong Kong; E-mail: wcliew@cse.cuhk.edu.hk; ityan@cityu.edu.hk

1573-4056/06 $50.00+.00

and possess a net spin. The human body is primarily fat and water, which have many hydrogen atoms. Medical MRI primarily images the NMR signal from the hydrogen nuclei in the body tissues.

The net spin of the nucleus around its axis gives it an angular moment. Since the proton is a positive charge, a current loop perpendicular to the rotation axis is also created, and as a result the proton generates a magnetic field. The joint effect of the angular moment and the self generated magnetic field gives the proton a magnetic dipole moment parallel to the rotation axis. Under normal condition, one will not experience any net magnetic field from the volume since the magnetic dipole moments are oriented randomly and on average equalize one another.

When placed in a magnetic field, a proton with its magnetic dipole moment precesses around the field axis. The frequency of this precession, v_0, is the resonant frequency of NMR and is called the Larmor frequency. The precession frequency is directly proportional to the strength of the magnetic field, i.e.

$$v_0 = \gamma B_0 \quad (1)$$

where B_0 is the main magnetic field strength, and γ is a constant called gyromagnetic ratio which is different for each nucleus (42.56 MHz/Tesla for protons).

Given a specimen, the application of a magnetic field B_0 would create a net equilibrium magnetization M_0 per cubic centimeter, which is aligned to the B_0 field. The M_0 is the net result of summing up the magnetic fields due to each of the H nuclei and is directly proportional to the local proton density (or spin density). However, M_0 is many orders of magnitude weaker than B_0 and is not directly observable. By tipping M_0 away from the B_0 field axis with an appropriate RF pulse having a frequency equals to the Larmor frequency, a longitudinal magnetization component M_L and a transverse magnetization component M_T is produced. When the RF pulse is turned off, the longitudinal magnetization component M_L recovers to M_0 with a relaxation time T_1, and the transverse magnetization component M_T dephases and decays to zero with a relaxation time T_2 [1]. During relaxation, the protons lose energy by emitting their own RF signal with the amplitude proportional to M_T. This signal is referred to as the *free-induction decay* (FID) response signal. T_2 indicates the time constant required for the FID response signal from a given tissue type to decay. The FID response signal is measured by an RF coil placed around the object being imaged.

To obtain a 3D MR image, the positional information about the tissues must be recorded. This involves isolating the source of each component of the MR signal to a particular voxel using the technique of spatial encoding. In MR imaging, spatial encoding is achieved by performing slice selection in one direction (e.g. the z-axis), frequency encoding in another direction (e.g. the x-axis), and phase encoding in the third direction (e.g. the y-axis). In slice selection, an RF excitation pulse with a narrow bandwidth is applied in the presence of a z-axis linear gradient field. Since the resonance frequency of a proton is proportional to the applied magnetic field, the presence of a gradient field means that only a narrow slice in the body will have a resonant frequency within the bandwidth of the RF pulse. Only the magnetization in this slice would be tipped by the RF pulse and produce the MR signal.

In the imaging sequence a phase encoding gradient is applied for a short interval after the slice selection gradient. When this is applied along the y-axis, the local magnetization is marked with a phase offset proportional to its y-position. Once the phase encoding gradient pulse is turned off, a frequency encoding gradient pulse is turned on. The frequency encoding gradient causes the precession of the local magnetization to vary linearly along the *x*-axis. Data acquisition then completes one phase-encoding step. The full two-dimensional (2D) image acquisition typically requires 128 or 256 phase-encoding steps, where for each step, the amplitude of the y gradient is increased in a regular fashion. The phase encoding and frequency encoding processes fill up the k-space with data. Each horizontal line in the k-space is obtained by readout during frequency encoding from one phase encoding step. The MR image is finally obtained by applying 2D inverse Fourier transform to the k-space data. In some cases, the k-space is sampled non-uniformly or portion of the k-space data is missing. Then more sophisticated techniques would be needed to reconstruct the image from incomplete information [13-15]. A 3D image can be obtained from many consecutive 2D slices.

A quantitative description of the MR signal produced by a particular tissue depends on at least three intrinsic tissue parameters: the proton density, which determines M_0, and the relaxation times T_1 and T_2. For example, at a magnetic field of 1.5T, $T_1 \approx 900\,ms$ for GM, $T_1 \approx 700\,ms$ for WM, and $T_1 \approx 4000\,ms$ for CSF. For the T_2 relaxation process (which is generally unrelated to the field strength), the time constants are approximately: 70ms, 90ms, and 400ms for WM, GM, and CSF, respectively [1].

When MR images are acquired, the RF pulse is repeated at a predetermined rate. The period of the RF pulse sequence is the *repetition time*, *TR*. The FID response signals can be measured at various times within the *TR* interval. The time between which the RF pulse is applied and the response signal is measured is the *echo delay time*, *TE*. The *TE* is the time when the spin echo occurs due to the refocusing effects of the 180 degree refocusing pulse applied after a delay of *TE*/2 from the RF pulse. The *TR* and *TE* control how strongly the local tissue relaxation times, T_1 and T_2, affect the signal. By adjusting *TR* and *TE* the acquired MR image can be made to contrast different tissue types.

3. THE MRI TISSUE SEGMENTATION PROBLEM

The task of image segmentation can be stated as the partition of an image into a number of non-overlapping regions, each with distinct properties. Using this definition, an image A can be modeled as the union of c homogeneous regions A_k,

[1] The actual decay time constant, T_2^*, is much shorter than T_2 due to the constant field offset caused by the magnetic field inhomogeneity in B_0, in addition to just the random spin-spin interaction in pure T_2 decay.

$$A = \bigcup_{k=1}^{c} A_k \quad (2)$$

where each homogeneous region is specified by the representative properties p_k, for example, signal intensity, and an additive, zero mean random noise component n_k,

$$A_k (x, y) = p_k + n_k \quad (3)$$

Each homogeneous region can consist of a single connected component or a group of possibly disjoint connected components of pixels with similar property. In (3), we assume that p_k is spatial invariant. When noise is not present or not severe, the segmentation task is straightforward, since we only need to estimate p_k and we have A_k $(x, y) = A_k$. Complication arises when p_k is not spatial invariant but instead is a function of location, since we now need a description of A_k (x, y) that is dependent on the location (x, y).

MR image segmentation involves the separation of image voxels into regions comprising different tissue types. Let $\underline{x} = (x, y, z)$ be the 3D image coordinate of a voxel. We assume that each tissue class k has a specific feature value v_k. For example, v_k could be the signal intensities that correspond to the tissue class being measured in the T_1, T_2, or PD weighted MR images. Then, the ideal signal $o(\underline{x})$ would consist of piecewise constant regions[2], each having one of the v_k values. Although this treatment is somewhat over-simplified since there is often biological variation even within the same tissue type, we assume that this intra-tissue biological variation is not overwhelming for the segmentation task.

MR images are often degraded by different artifacts for a variety of reasons. The artifact that is of major concern to many MRI segmentation algorithms is the so-called intensity non-uniformity artifact [16]. The INU artifact arises due to inhomogeneity in the magnetic field, and manifests itself as an unwanted low frequency bias term modulating the signal. The cause is usually due to either a non-uniform B_1 field or a non-uniform sensitivity in the receiver coil. The inhomogeneity could also be caused by the interaction of the acquisition system with the patient such as RF attenuation. RF coil field strength inhomogeneity can yield intensity variations on the order of 10-20% in image amplitudes over the patient volume on a 1.5T magnet. The problem becomes even more pronounced at higher field strength. While such variations usually have no effect on diagnostic accuracies, they do cause significant problems for segmentation and statistical clustering tasks that are based on voxel intensity distributions. When such intensity variation becomes significant compared to the image contrast, it can easily affect the interpretation of an MR image.

The bias field that gives rise to the INU artifact in an MR image is usually modeled as a smooth slow-varying multiplicative field (see [17-22]). The image formation process in MRI can thus be modeled as,

$$s(\underline{x}) = o(\underline{x})b(\underline{x}) + n(\underline{x}) \quad (4)$$

[2] In practice, the limited resolution of the imaging device leads to blurring along border regions between tissue classes, i.e., the partial volume effect. However, this effect is confined to the border regions, in contrast to the more global INU artifact.

where $s(\underline{x})$ is the measured MR signal, $o(\underline{x})$ is the true signal emitted by the tissue, $b(\underline{x})$ is the unknown smoothly varying bias field, and $n(\underline{x})$ is an additive noise assumed to be independent of $b(\underline{x})$. Accurate segmentation of an MR image thus requires an accurate estimation of the unknown bias field $b(\underline{x})$ and removing this bias field from the measured MR signal prior to or during segmentation. Using the estimated $b(\underline{x})$, the log-transformed true signal can be recovered as

$$\begin{aligned} \log \tilde{o}(\underline{x}) &= \log s(\underline{x}) - \log \tilde{b}(\underline{x}) \\ &\approx \log(o(\underline{x}) + n(\underline{x}) / \tilde{b}(\underline{x})) \end{aligned} \quad (5)$$

Another MR imaging artifact that affects tissue delineation is the partial volume averaging (PVA) artifact [23-25]. PVA artifact occurs when multiple tissues are present in one voxel due to the limited resolution of the imaging device. The PVA artifact is particularly noticeable in the extreme slices of MRI volumes. The intensity of a voxel affected by PVA is a weighted average of the intensities of the different tissues in the voxel, and fine anatomical structures are lost in the image. PVA affects the accuracy of delineation and volume estimation of different tissue types, which could be critical in the diagnosis and analysis of pathology.

All MR images are affected by random noise. The noise comes from the stray currents in the detector coil due to the fluctuating magnetic fields arising from random ionic currents in the body, or the thermal fluctuations in the detector coil itself. When the level of noise is significant in an MR image, tissues that are similar in contrast could not be delineated effectively, causing errors in tissue segmentation.

4. 3D MR BRAIN IMAGE TISSUE SEGMENTATION TECHNIQUES

Brain tissue segmentation is usually concerned with the delineation of 3 types of brain matters, i.e., GM, WM and CSF. Because most brain structures are anatomically defined by boundaries of these tissue classes, accurate segmentation of brain tissues into one of these categories is an important step in quantitative morphological study of the brain. In this section, we give a succinct review of several different approaches for MR brain image segmentation under three broad algorithmic frameworks, namely, classification-based, region-based, and contour-based approaches. A more detail review of our own approach is also given in this section.

4.1. Classification-Based Segmentation

In classification-based segmentation, voxels are classified and labeled as belonging to a particular tissue class according to a certain criterion. The simplest technique is based on thresholding [26-29]. Thresholding algorithm attempts to determine a threshold value which separates the desired classes. In [26], Suzuki and Toriwaki use iterative thresholding to distinguish brain tissues from others in axial MR slices. Starting at set values, thresholds for the head and the brain are then iteratively adjusted based on the geometry of resulting masks. Although thresholding algorithm is simple and computationally very fast, it is very sensitive to INU artifact and noise in MR images. The automatic determination of a suitable threshold could be problematic if

there is severe overlap between the intensities of different tissue types due to noise and intensity inhomogeneities.

Instead of using simple thresholding in earlier classification-based segmentation work, statistical classification based segmentation has been the method of choice in more recent time. Statistical classification has the advantage of being more robust, as well as having a rigorous mathematical foundation in stochastic theory. In statistical classification methods, the probability density function of tissue intensity for different tissue classes are often modeled parametrically as a mixture of Gaussians, usually one Gaussian function per tissue class. In order to incorporate local contextual information, Markov random field (MRF) regularization is often employed as well. The MRF regularization allows one to model the spatial interactions between neighboring voxels. In [20], Wells *et al*. describe an iterative method that interleaves classification with bias field correction. The bias field estimation problem is cast in a Bayesian framework and the expectation-maximization (EM) algorithm is used to estimate the inhomogeneity and the tissue classes. However, their method needs to be supplied with the tissue class conditional intensity models, which are typically constructed manually from training data. They also did not consider neighborhood dependencies for the tissue segmentation. In [30], Held *et al*. improved on Wells *et al*.'s algorithm by using MRF to introduce context or dependency among neighboring voxels. In [31, 32], Leemput *et al*. propose to use a 3-step EM algorithm, which interleaves voxel classification, class distribution parameter estimation, and bias field estimation. Instead of using manually constructed tissue class conditional intensity models, their method employs digital brain atlas with a priori probability maps for each tissue class to automatically construct intensity models for each individual scan being processed. The brain tissue classes are modeled as finite Gaussian mixtures with MRF regularization to account for contextual information and the bias field is modeled as a fourth order least square polynomial fit. In [33], Rajapakse *et al*. also use the Gaussian mixture to model the three brain tissue classes. The biological variations of a particular tissue class are accounted for in their statistical model by assuming that the mean intensities of the tissue classes are slowly varying spatial functions. The magnetic field inhomogeneities modify both the mean tissue intensities and the noise variances in a similar manner. To account for the smoothness and piecewise contiguous nature of the tissue regions, they use a 3D MRF as a prior. In [34], Desco *et al*. consider the statistical segmentation of multispectral MR brain image. In their work, the intensity distributions of the brain tissues are again modeled as a mixture of Gaussians. They use a robust version of the EM algorithm called logistic EM algorithm to estimate the model parameters, and use MRF to incorporate prior knowledge into the segmentation process.

Another major class of voxel classification techniques uses clustering-based method. Clustering is a popular unsupervised classification method and has found many applications in pattern classification and image segmentation [35-46]. Clustering algorithm attempts to classify a voxel to a tissue class by using the notion of similarity to the class. The fuzzy c-means clustering (FCM) algorithm has recently been applied to MRI segmentation [9, 43-46]. Unlike the crisp k-means clustering algorithm [41, 42], the FCM algorithm allows partial membership in different tissue class. Thus, FCM can be used to model the PVA artifact, where a voxel may contain multiple tissue classes [44]. A method of simultaneously estimating the INU artifact and performing voxel classification based on fuzzy clustering has been reported in [45], where intermediate segmentation results are utilized for the INU estimation. The method uses a modified FCM cost functional to model the variation in intensity values and the computation of the bias field is formulated as a variational problem. However, in conventional FCM clustering algorithm, there is no consideration of spatial context between voxels since the clustering is done solely in the feature space. We have recently proposed a novel adaptive fuzzy clustering algorithm for MRI segmentation that takes into account both the INU artifact and the spatial correlation between neighboring pixels [46]. A more detail description of the ideas in our clustering-based MRI segmentation algorithm will be given in Section 4.5.

4.2. Region-Based Segmentation

The shape of an object can be described in terms of its boundary or the region it occupies. Image region belonging to an object generally have homogeneous characteristics, e.g. similar in intensity or texture. Region-based segmentation techniques attempt to segment an image by identifying the various homogeneous regions that correspond to different objects in an image. Unlike clustering methods, region-based methods explicitly consider spatial interactions between neighboring voxels. In its simplest form, region growing methods usually start by locating some seeds representing distinct regions in the image [47, 48]. The seeds are then grown until they eventually cover the entire image. The region growing process is therefore governed by a rule that describe the growth mechanism and a rule that check the homogeneity of the regions at each growth step.

Region growing technique has been applied to MRI segmentation [49-51]. In [49], a semi-automatic, interactive MRI segmentation algorithm was developed that employ simple region growing technique for lesion segmentation. In [50], an automatic statistical region growing algorithm based on a robust estimation of local region mean and variance for every voxel on the image was proposed for MRI segmentation. The best region growing parameters are automatically found via the minimization of a cost functional. Furthermore, relaxation labeling, region splitting, and constrained region merging were used to improve the quality of the MRI segmentation. The determination of an appropriate region homogeneity criterion is an important factor in region growing segmentation methods. However, such homogeneity criterion may be difficult to obtain a priori. In [51], an adaptive region growing method is proposed where the homogeneity criterion is learned automatically from characteristics of the region to be segmented while searching for the region.

Other region-based segmentation techniques, such as split-and-merge based segmentation [52] and watershed-based segmentation [53, 54] have also been proposed for MRI segmentation. In the split-and-merge technique, an image is first split into many small regions during the splitting stage according to a rule, and then the regions are

merged if they are similar enough to produce the final segmentation. In [53], Sijbers *et al.* used the watershed algorithm to segment MR images. In the watershed-based segmentation, the gradient magnitude image is considered as a topographic relief where the brightness value of each voxel corresponds to a physical elevation. An immersion based approach is used to calculate the watersheds. The operation can be described by imagine that holes are pierced in each local minimum of the topographic relief. Then, the surface is slowly immersed in water, which causes a flooding of all the catchment basins, starting from the basin associated with the global minimum. As soon as two catchment basins begin to merge, a dam is built. The procedure results in a partitioning of the image in many catchment basins of which the borders define the watersheds. To reduce over-segmentation, the image is smoothed by 3D adaptive anisotropic diffusion prior to watershed operation. Semi-automatic merging of volume primitives returned by the watershed operation is then used to produce the final segmentation.

4.3. Contour-Based Segmentation

Contour-based segmentation approach assumes that the different objects in an image can be segmented by detecting their boundaries. Whereas region-based techniques attempt to capitalize on homogeneity properties within regions in an image, boundary-based techniques rely on the gradient features near an object boundary as a guide. Hence, contour-based segmentation methods that rely on detecting edges in the image is inherently more prone to noise and image artifacts. Sophisticated pre- and post-processing is often needed to achieve a satisfactory segmentation result. The simplest contour-based technique is edge detection. MR image segmentation based on edge detection has been proposed in [55], where a combination of Marr-Hildreth operator for edge detection and morphological operations for the refinement of the detected edges is used to segment 3D MR images. In [56], a boundary tracing method is proposed, where the operator clicks a pixel in a region to be outlined and the method then finds the boundary starting from that point. The method is, however, restricted to segmentation of large, well defined structures, but not to distinguish fine tissue types. Edge-based segmentation methods usually suffer from over or under-segmentation, induced by improper threshold selection [57]. In addition, the edges found are usually not closed and complicated edge linking techniques are further required.

Another approach for contour-based segmentation is based on the deformable templates or active contours [58-63]. Active contour deforms to fit the object's shape by minimizing (among others) a gradient dependent attraction force while at the same time maintaining the smoothness of the contour shape. Thus, unlike edge detection, active contour methods are much more robust to noise as the requirements for contour smoothness and contour continuity act as a type of regularization. Another advantage of this approach is that prior knowledge about the object's shape can be built into the contour parameterization process. However, active contour based algorithms usually require initialization of the contour close to the object boundary for it to converge successfully to the true boundary. More importantly, active contour methods have difficulty handling deeply convoluted boundary such as CSF, GM and WM boundaries due to their contour smoothness requirement. Hence, they are often not appropriate for the segmentation of brain tissues. Nevertheless, it has been applied successfully to the segmentation of intracranial boundary [60], brain outer surface [61], and neuro-anatomic structures in MR brain images [62].

4.4. Other Approaches

There are segmentation algorithms that attempt to incorporate knowledge about brain anatomy into the segmentation process. Such knowledge-based a priori information, if applied appropriately, can significantly improve the accuracy of the final segmentation results. Atlas-guided segmentations are a powerful tool for MRI segmentation when a standard atlas or template is available. The atlas is generated by compiling information on the anatomy that requires segmentation. This atlas is then used as a reference frame for segmenting new images. Atlas-based methods view the segmentation problem as a registration problem. The basic tenet of these techniques is that a transformation can be found that registers one image volume (called the reference or the atlas) in which structures of interest have been labeled to the volume to be segmented [64]. If such a transformation can be computed, regions labeled in the atlas can simply be projected onto the volume of interest. A difficulty with the atlas approach is to determine an accurate and robust registration, especially for complex structures. This problem is non-trivial owing to the anatomical variability. Thus, atlas-guided segmentations are generally better suited for segmentation of structures that are stable over the population of study.

Atlas guided approaches have been applied in MR brain imaging for segmentation of various structures [65], as well as for extracting the brain volume from head scans [66]. Arata *et al*. [67] registered individual patient data sets to an atlas to determine inter-patient variability. Dawant *et al*. [64] used a global transformation of an atlas data set in combination with free-form transformations to segment MR images. In [68], a probabilistic atlas is used to model the anatomical variability in MR brain images.

Machine learning approach such as artificial neural networks (ANNs) has also been used in MRI segmentation [43, 69-72]. ANNs are parallel networks of processing elements or nodes that simulate biological learning. Each node in an ANN is capable of performing elementary computations. Learning is achieved through the adaptation of weights assigned to the connections between nodes. Because of the many interconnections used in neural network, spatial information can be easily incorporated into its classification procedures. The availability of an efficient learning algorithm and a representative learning set are the main concern of machine learning-based approaches.

4.5. A Novel FCM-based Adaptive Segmentation Method

We have recently proposed an FCM-based adaptive MRI segmentation algorithm that addresses both the INU artifact and the local spatial context [46]. Our approach contains two key ideas: (1) we incorporate the local spatial context into the FCM algorithm using a novel dissimilarity index in place of the usual distance metric; and (2) we make the cluster

prototype spatially varying by applying a 3D multiplicative bias field to it.

At the core of our algorithm is the FCM clustering algorithm. The FCM clustering algorithm assigns a class membership to a data point, depending on the similarity of the data point to a particular class relative to all other classes [35]. In term of image segmentation, the FCM procedure is able to perform soft segmentation, where pixels or voxels can be classified into more than one classes with varying degree of membership. This behavior is beneficial for MR image segmentation, since noise and PV effect make the exclusive assignment of voxels to distinct classes undesirable.

The conventional FCM algorithm is formulated as the minimization of the objective functional J_{FCM} with respect to the membership values U and cluster centroids V,

$$J_{FCM}(U,V) = \sum_{\underline{x}\ I}\sum_{k=1}^{c} u_{k\underline{x}}^{m} d_{k\underline{x}}^{2} \qquad (6)$$

subject to the constraint $\sum_{k=1}^{c} u_{k\underline{x}} = 1 \quad \underline{x} \quad I$

where the matrix U = $\{u_{k\underline{x}}\}$ is a fuzzy c-partition of S, V = $\{v_1, v_2,\ldots, v_c\}$ is the set of fuzzy cluster centroids, m (1,∞) is the fuzzy index, c is the total number of clusters, and $u_{k\underline{x}}$ gives the membership of pixel $s(\underline{x})$ in the k-th cluster c_k.. The distance metric $d^2_{k\underline{x}} = ||s(\underline{x}) - v_k||^2$ in (6) measures the vector distance of a feature vector from a cluster centroid v_k in the feature space.

In the conventional FCM formulation, each class is assumed to have a constant value as given by its centroid. Each data point is also assumed to be independent of every other data point and independent of their spatial coordinates. However, for MR images, there is strong correlation between neighboring voxels. For example, neighboring voxels would be similar in attributes if they belong to the same sub-volume from one tissue type and are generally not independent of each other. The incorporation of local spatial interaction between adjacent voxels in the fuzzy clustering process can produce more meaningful classification, as well as help to resolve classification ambiguities due to overlap in intensity value between clusters or due to noise corruption. In addition, due to the INU artifact, the data in a class no longer have a constant value but is dependent on its spatial position in the image. Therefore, to produce meaningful segmentation, the conventional FCM algorithm has to be modified to take into account both the local spatial context between neighboring voxels and the INU artifact.

Our idea of incorporating local spatial context into the FCM algorithm is to replace the distance metric $d^2_{k\underline{x}}$ in (6) by a novel dissimilarity index $D_{k\underline{x}}$ [38]. Let Àp denote a chosen 3D local neighborhood configuration with respect to a center voxel ρ. Let $dist(a,b) = \sqrt{\|a-b\|^2}$ denote the L_2 distance between vectors a and b. For every pixel $s(\underline{x})$ in the 3D MR image, we define the following L_2 distances,

$$\partial_{\underline{xy}} = dist(s(\underline{x}), s(\underline{y})),\ s(\underline{y}) \quad \grave{A}_{\underline{x}}, \qquad (7)$$

$$d_{k\underline{x}} = dist(s(\underline{x}), v_k), \qquad (8)$$

where $\grave{A}_{\underline{x}}$ is the neighborhood of $s(\underline{x})$ and v_k is the centroid of the k-th cluster. The first distance metric $\partial_{\underline{xy}}$ measures the dissimilarity of the pixel $s(\underline{x})$ and its neighbor $s(\underline{y})$. The second distance metric $d_{k\underline{x}}$ measures the affinity of the center pixel $s(\underline{x})$ to the cluster prototype v_k. Taking all voxels in $\grave{A}_{\underline{x}}$ into account, the dissimilarity index $D_{k\underline{x}}$ which measures the dissimilarity between $s(\underline{x})$ and the k-th cluster centroid v_k is defined as

$$D_{k\underline{x}} = \frac{1}{|\grave{A}_{\underline{x}}|}\sum_{\underline{y}\ \grave{A}_{\underline{x}}}\left[d^2_{k\underline{x}}\lambda_{\underline{xy}} + d^2_{k\underline{y}}(1-\lambda_{\underline{xy}})\right] \qquad (9)$$

where ½À$_{\underline{x}}$½ is the cardinality of the neighborhood configuration, and $\lambda(\partial_{\underline{xy}}) = \lambda_{\underline{xy}}$, with ranges between zero and one, is the weighting factor controlling the degree of influence of the neighboring voxels $s(\underline{y})$ À$_{\underline{x}}$ on the center voxel $s(\underline{x})$. The weighting factor provides a convex combination of the two cluster affinity distances $d_{k\underline{x}}$ and $d_{k\underline{y}}$ in an adaptive manner, and is given by

$$\lambda(\partial) = \frac{1}{1+e^{-(\partial-\mu)/\sigma}} \qquad (10)$$

where the parameters μ and σ specify the displacement of λ from zero, and the steepness of λ, respectively. It is not difficult to see that the new index $D_{k\underline{x}}$ is adaptive to the local image content, i.e., at genuine edges or object boundaries, spatial interaction is turn off, while at homogenous regions, interaction between neighboring voxels is very significant. Several additional observations can also be made about our FCM formulation using $D_{k\underline{x}}$: (1) It has a noise suppression capability due to the adaptive smoothing operation; and (2) It takes into account explicitly the spatial dimensionality of the data due to the chosen local neighborhood configuration. This is in contrast to the conventional FCM algorithm, where each data point is viewed as an independent instance, regardless of whether the data are from 2D, 3D, or from N-D space.

As we mentioned before, the INU artifact manifests itself as a slow varying multiplicative bias field. Hence, we accommodate that into the clustering algorithm by making the cluster prototype adaptive to the spatial position. Specifically, we let the $d^2_{k\underline{x}}$ in (9) be replaced by

$$d^2_{k\underline{x}} = \left\|\hat{s}(\underline{x}) - w(\underline{x}) - \hat{v}_k\right\|^2 \qquad (11)$$

where $w(\underline{x})$ is the log bias field, $s(x)$ = log $s(x)$ and v_k =log v_k. This is equivalent to estimating the bias field in the log domain. For computational efficiency, we model the 3D bias field as a stack of 2D smoothing B-spline surfaces, with continuity explicitly enforced between adjacent surfaces. The 2D log bias field $w_z(x,y)$ at index z is formed by the tensor products of cubic B-spline bases, i.e.,

$$w_z(x,y) = \sum_{i=-3}^{g}\sum_{j=-3}^{h}\alpha_{ij}^{z} N_{i,4}(x) M_{j,4}(y) \qquad (12)$$

Now, estimating the bias field becomes that of estimating the cubic *B*-spline coefficients. Such a formulation has the advantage that the number of spline coefficients to be estimated is much less than the number of voxels in the bias field. The estimated bias field would also be very smooth due to the explicit spline modeling.

With the above two modifications, our fuzzy clustering algorithm for MRI segmentation can be formulated as the solution $\{U^*, v^*, w^*\}$ that minimizes

$$J_{ASFCM} = \sum_{\underline{x} \in I} \sum_{k=1}^{c} u_{k,\underline{x}}^{m} D_{k,\underline{x}} + \beta \eta(w_z(x,y)) + \gamma \phi(w_z(x,y)) \quad (13)$$

subject to $$\sum_{k=1}^{c} u_{k,\underline{x}} = 1 \qquad \underline{x} \in I$$

where the first regularizing term is given by

$$\eta(w_z(x,y)) = \iint \left[\left(\frac{\partial^2 w_z(x,y)}{\partial x^2} \right)^2 + 2 \left(\frac{\partial^2 w_z(x,y)}{\partial x \partial y} \right)^2 + \left(\frac{\partial^2 w_z(x,y)}{\partial y^2} \right)^2 \right] dxdy \quad (14)$$

and the second regularizing term is given by

$$\phi(w_z(x,y)) = \iint \left(\frac{\partial^2 w_z(x,y)}{\partial z^2} \right)^2 dxdy \quad (15)$$

The first regularizing term minimizes the thin plate energy of each of the spline surfaces $w_z(x,y)$. The second regularizing term forces smoothness between slices of spline surfaces. It couples the slices together to form a smooth 3D field. Iterative minimization of (13) will give us the solution to our MRI segmentation problem.

We implemented our algorithm in C language and tested it on both simulated 3D MR brain images obtained from the BrainWeb Simulated Brain Database at the McConnell Brain Imaging Centre of the Montreal Neurological Institute (MNI), McGill University [73-76], and on real MRI data. Our algorithm is computationally very efficient. For the simulated 3D MRI brain image of dimension 217x181x181 (row (y) × column (x) × depth (z)), the total computation time is around 1.5 to 2 minutes on a Pentium-4 2GHz PC. We presented some segmentation results on the simulated 3D MR brain images below to show the efficacy of our approach.

Fig. (**1**) shows a slice of the simulated 3D MR brain image. Fig. (**2a**) shows the segmented image. The segmentation can be observed to correspond well to the true model. Fig. (**2b**) shows the recovered bias field, which resembles very closely the actual bias field in Fig. (**1c**). In comparison, we also show in Fig. (**2c**) the segmentation by the conventional FCM algorithm, whose accuracy is severely affected by noise and INU. Note the poor segmentation of WM and GM around the lower left part of the brain where the INU artifact is most severe. The results clearly indicate that the proposed algorithm is able to compensate for noise and INU artifact in the input image. Fig. (**3a**) shows an across-slice view of the actual bias field, taken at $y = 110$, for the same data set. Fig. (**3b**) shows the estimated bias field taken at the same location. As can be seen, the estimated bias field has captured accurately the intensity inhomogeneity across slices without exhibiting between-slice discontinuity in spite of the modeling of the 3D bias field by a stack of 2D spline surfaces. Fig. (**4**) shows the 3D renderings of the WM segmented using our algorithm (middle image) and using the conventional FCM algorithm (bottom image). The ground truth is shown in the top image. Comparing the segmented results with the ground truth (see Fig. (**4**)), it is obvious that our algorithm gives a much more accurate segmentation result - the degradation when INU artifact is not compensated for is especially noticeable around the base of the brain, at the top of the brain, and at the top end region of the transverse view.

For quantitative evaluation, our method has significantly better performance than several existing state-of-the art methods and is more robust to increased inhomogeneities. For the simulated MRI data (T_1 weighted, 1 mm^3 voxels, 3% noise) with varying level of INU inhomogeneity (i.e., 0%

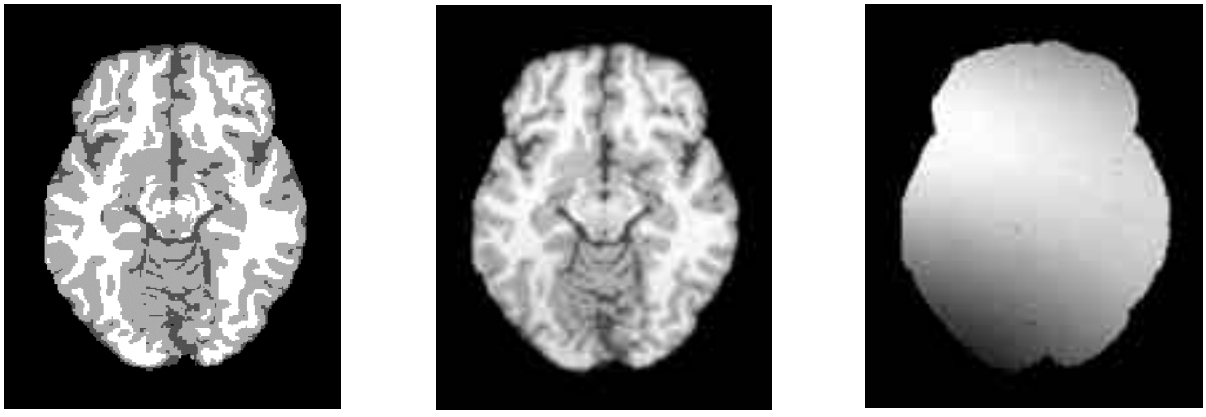

(**a**) (**b**) (**c**)

Fig. (1). A slice of the simulated 3D brain image from MNI ($z = 60$). (a) True model. (b) Image corrupted with noise and INU artifact. (c) The corresponding bias field.

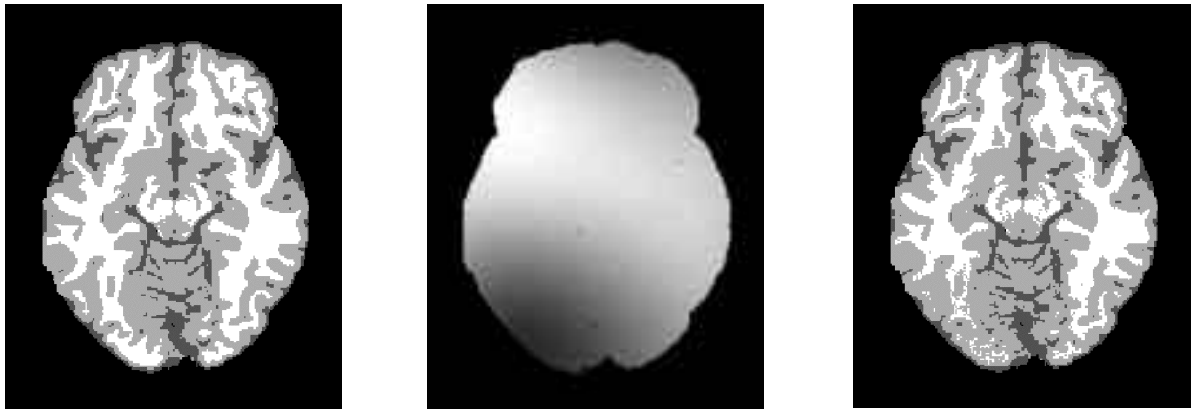

(**a**) (**b**) (**c**)

Fig. (2). Segmentation result for the MRI image of Fig.1(b). (a) The segmentation using the proposed algorithm. (b) The recovered bias field. (c) The segmentation using the conventional FCM algorithm without taking into account spatial context and INU compensation.

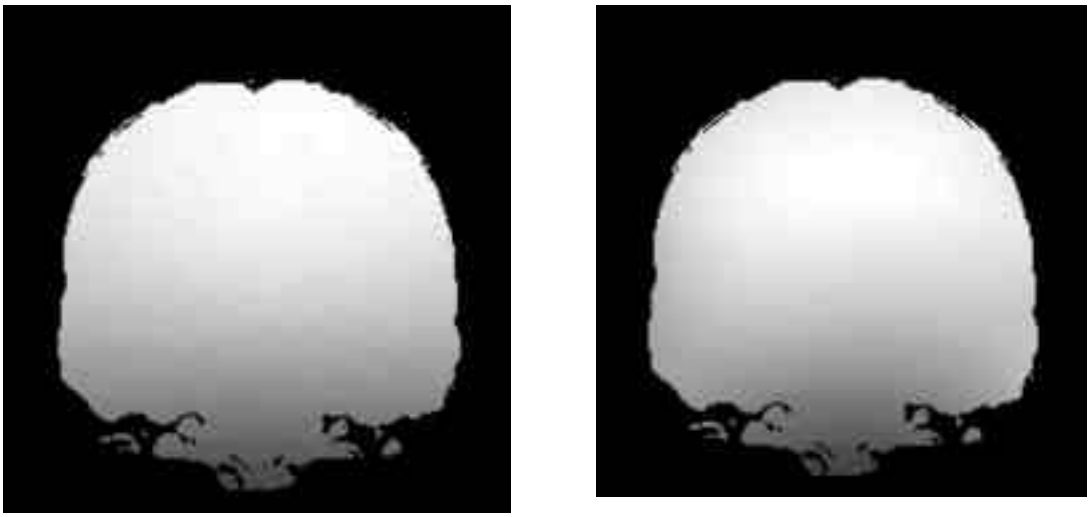

(**a**) (**b**)

Fig. (3). (a) Actual, and (b) computed bias field for $y = 110$. The x coordinate increases from left to right and the z coordinate increases from bottom to top.

INU, 20% INU, 40% INU), our algorithm consistently achieves a misclassification rate (MCR) of less than 4%. The MCR is defined to be the number of pixels misclassified by the algorithm divided by the total number of pixels in the three tissue classes in the image. The interested reader is referred to our work in [46] for the detail quantitative comparison.

Due to the limited resolution of the imaging device, it is possible that multiple tissues are present in one voxel, giving rise to the PVA artifact. FCM-based methods are able to perform a soft segmentation of the MR images, where the tissue membership value indicates the contribution of each tissue to a voxel. We use the tissue membership values to perform PV estimation. Since in 3D volume, the interface between two tissues forms a surface, whereas the interface between three tissues forms a line, PVA is therefore much more frequent between two tissue types. We modify the membership values returned by our algorithm to reflect this observation. Fig. (**5**) shows the results of PV estimation. The second to the fifth row of Fig. (**5**) shows the results of soft segmentation for GM, WM, and CSF for our algorithm, the FCM algorithm, and the EM-MRF algorithms of Leemput *et al*. [31, 32] without and with MRF regularization, respectively. By comparing to the ground truth at the first row, it is clear that our algorithm can estimate the PV much more accurately than the other three algorithms. The PV estimations given by the FCM algorithm suffer from INU artifact and noise, whereas the PV estimations given by the EM-MRF algorithms either do not model the PVA accurate enough or suffer from perimeter shading. The perimeter shading is particularly noticeable in the GM PV estimation given by the EM-MRF algorithm with MRF regularization, and the CSF PV estimation given by the EM-MRF algorithm with and without MRF regularization. The detail quantitative results will be presented elsewhere.

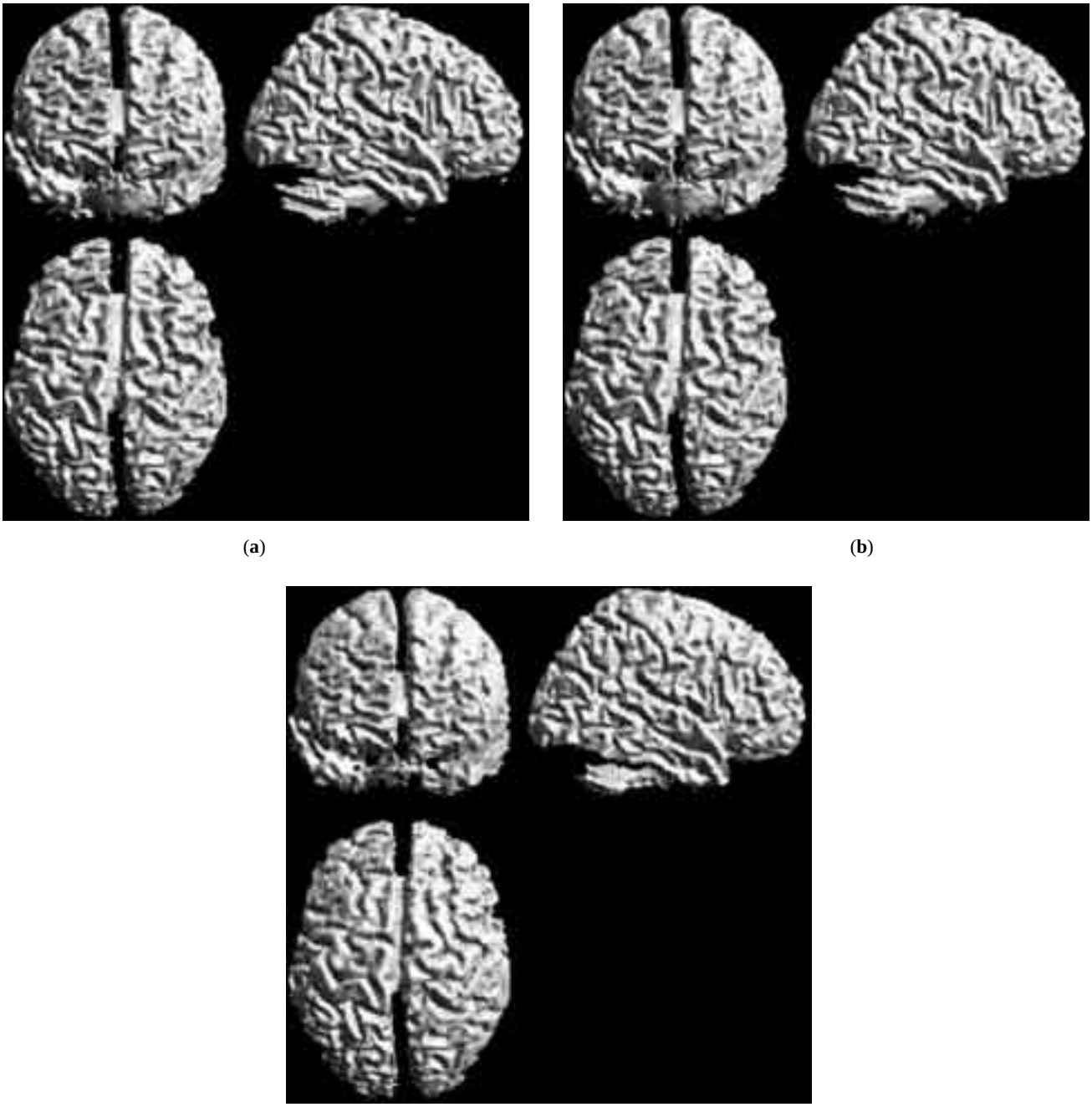

(**a**) (**b**)

(**c**)

Fig. (4). Three dimensional renderings of the WM: (top) the ground truth; (middle) segmented using our algorithm; (bottom) segmented using the conventional FCM algorithm. The simulated brain image is corrupted with 3% noise and 40% INU.

DISCUSSIONS AND CONCLUSIONS

The segmentation of MR brain images is an important problem in medical imaging. Although much effort has been spent on finding a good solution to the MRI segmentation problem, it is far from been solved [77]. This paper attempts to give an overview of the MR brain image segmentation problem and discusses various computational techniques for solving the problem. We reviewed segmentation algorithms that can be broadly categorized into classification-based, region-based, or contour-based approaches, and discussed the advantages and disadvantages of each category.

We also provided a succinct discussion of our recent adaptive spatial fuzzy c-means segmentation algorithm that takes into account the local spatial context, as well as the suppression of the INU artifact in 3D MR brain images. Our algorithm employs a novel dissimilarity index that considers the local influence of neighboring pixels in an adaptive manner. To suppress the INU artifact, a 3D multiplicative

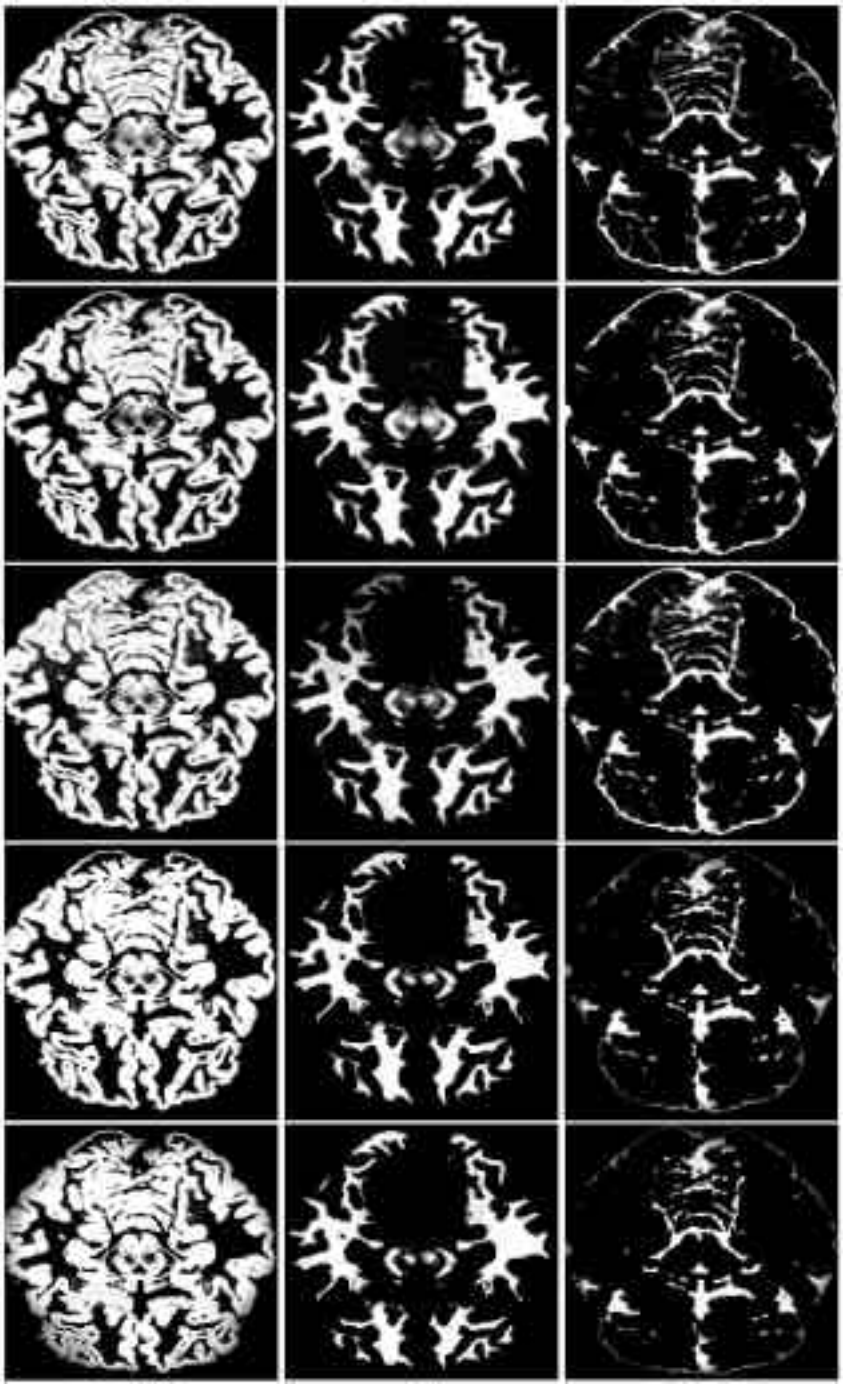

Fig. (5). Soft segmentation as an estimation of PV for GM, WM, and CSF. The top row is the true PV. The second to fifth rows are the PV estimation for our algorithm, FCM algorithm, EM-MRF without MRF regularization, and EM-MRF with MRF regularization, respectively.

bias field modeled using B-splines is estimated from the MR brain images during the clustering process. Due to the use of soft segmentation, our algorithm is also able to give a good estimation of tissue volume in the presence of PVA artifact.

Future research in MRI segmentation should strive toward improving the accuracy, precision, and computation speed of the segmentation algorithms, while reducing the amount of manual interactions needed. This is particularly important as MR imaging is becoming a routine diagnostic procedure in clinical practice. It is also important that any practical segmentation algorithm should deal with 3D volume segmentation instead of 2D slice by slice segmentation, since MRI data is 3D in nature. Volume segmentation ensures continuity of the 3D boundaries of the segmented images whereas slice by slice segmentation does not guarantee continuation of the boundaries of the tissue regions between slices.

In view of the vast amount of anatomical knowledge gained from past clinical studies, it would be advantageous for segmentation algorithms to efficiently utilize this prior knowledge. Although our approach and the MRF regularization are able to consider local spatial context, the prior knowledge that is utilized here is considered to be very low level knowledge. Higher level anatomical knowledge, if used appropriately, should boost the accuracy and robustness of the segmentation algorithm. A possible research direction is to find way to effectively exploit the anatomical knowledge about the brain into existing segmentation algorithms.

For segmentation methods to gain acceptance in routine clinical applications, extensive validation is required on the algorithms concerned. The setting up of an experiment protocol and a platform for algorithm validation would be invaluable in this case. This would require the availability of common databases where algorithms can be compared and contrasted to each other. Modest progress has been made in this area, for example, the simulated 3D MR brain images that we use for validation in our work are obtained from the BrainWeb Simulated Brain Database at the McConnell Brain Imaging Centre of the Montreal Neurological Institute, McGill University (http://www.bic.mni.mcgill.ca/brainweb) [74-76]. These simulated images have enabled us to perform quantitative evaluation of our algorithm against a ground truth. Nevertheless, there is still a lack of actual clinical databases for validation purposes. Much work is urgently needed in this avenue to systematically collect, annotate, and maintain a set of real test images that enables detail and fair evaluation and comparison between different algorithms.

ABBREVIATIONS

ANN	=	Artificial neural network
CSF	=	Cerebrospinal fluid
EM	=	Expectation-maximization
FCM	=	Fuzzy c-means clustering
GM	=	Gray matter
INU	=	Intensity nonuniformity
MR	=	Magnetic resonance
MRI	=	Magnetic resonance imaging
MRF	=	Markov random field
MCR	=	Misclassification rate
MNI	=	Montreal Neurological Institute
NMR	=	Nuclear magnetic resonance
PV	=	Partial volume
PVA	=	Partial volume averaging
RF	=	Radio-frequency
3D	=	Three-dimensional
2D	=	Two-dimensional
WM	=	White matter

REFERENCES

[1] Haacke EM, Brown RW, Thompson MR, Venkatesan R. Magnetic Resonance Imaging: Physical Principles and Sequence Design. Wiley, New York, 1999.

[2] Bedell BJ, Narayana PA. Automatic segmentation of gadolinium-enhanced multiple sclerosis lesions. Magnetic Resonance in Medicine 1998; 39(6): 935-40.

[3] Shenton ME, Kikinis R, Jolesz F, *et al*. Abnormalities of the left temporal lobe and thought disorder in schizophrenia. N. Eng. J. Med. 1992; 327(9): 604-12.

[4] McCarley RW, Wible CG, Frumin M, *et al*. MRI anatomy of schizophrenia. Biol. Psychiatry 1999; 45:1099-119.

[5] Lawrie SM, Abukmeil SS. Brain abnormality in schizophrenia - A systematic and quantitative review of volumetric magnetic resonance imaging studies. British Journal of Psychiatry 1998; 172:110-20.

[6] Tanabe JL, Amend D, Schuff N, *et al*. Tissue segmentation of the brain in Alzheimer disease. AJNR American Journal of Neuroradiology 1997; 18(1): 115-23.

[7] Kidron D, Black SE, Stanchev P, *et al*. Quantitative MR volumetry in Alzheimer's disease – Topographic markers and the effects of sex and education. Neurology 1997; 49(6): 1504-12.

[8] Rusinek H, DeLeon MJ, Goerge AE, *et al*. Alzheimer's disease: Measuring loss of cerebral gray matter with MR imaging. Radiology 1991; 178(1): 109–14.

[9] Bezdek J, Hall L, Clarke L. Review of MR image segmentation techniques using pattern recognition. Med. Physics 1993; 20(4): 1033-48.

[10] Clarke LP, Velthuizen RP, Camacho MA, *et al*. MRI segmentation: Methods and applications. Journal of Magnetic Resonance Imaging 1995; 13(3):343–68.

[11] Chakeres DW, Schmalbrock P. Fundamentals of Magnetic Resonance Imaging. Williams & Wilkins, Baltimore, 1992.

[12] Buxton RB. Introduction to Functional Magnetic Resonance Imaging-Principles and Techniques. Cambridge University Press, 2002.

[13] Yan H, Gore JC. An efficient algorithm for MR image reconstruction without low spatial frequencies. IEEE Trans. Med. Imag. 1990; TMI-9:184-9.

[14] Yan H, Braun M. Image reconstruction from Fourier domain data sampled along a zig-zag trajectory. Magnetic Resonance in Medicine 1991; 18:405-10.

[15] H. Yan (ed). Signal Processing in Magnetic Resonance Imaging and Spectroscopy. Marcel Dekker Inc., 2002.

[16] Sled JG, Pike GB. Understanding intensity nonuniformity in MRI. Proc. Medical Image Computing Computer-Assisted Intervention-MICCAI'98 (Lecture Notes in Computer Science). Berlin, Germany: Springer-Verlag, 1998; 1496: 614-22.

[17] Meyer CR, Bland PH, Pipe J. Retrospective correction of intensity inhomogeneities in MRI. IEEE Trans. Med. Imag. 1995; 12: 36-41.

[18] Dawant BM, Zijdenbos AP, Margolin RA. Correction of intensity variations in MR images for computer-aided tissue classification. IEEE Trans. Med. Imag. 1993; 12: 770-81.

[19] Sled JG, Zijdenbos AP, Evans AC. A nonparametric method for automatic correction of intensity nonuniformity in MRI data. IEEE Trans. Med. Imag. 1998; 17: 87-97.

[20] Wells III WM, Grimson WEL, Kikinis R, Jolesz FA. Adaptive segmentation of MRI data. IEEE Trans. Med. Imag. 1996; 15: 429-42.

[21] Tincher M, Meyer CR, Gupta R, Williams DM. Polynomial modeling and reduction of RF body coil spatial inhomogeneity in MRI. IEEE Trans. Med. Imag. 1993; 12: 361-5.

[22] Styner M, Brechbuhler C, Szekely G, Gerig G. Parametric estimate of intensity inhomogeneities applied to MRI. IEEE Trans. Med. Imag. 2000; 9: 153-65.

[23] Choi HS, Haynor DR, Kim Y. Partial volume tissue classification of multichannel magnetic resonance images-a mixel model. IEEE Trans Med. Imag. 1991; 10(3): 395-407.

[24] Laidlaw DH, Fleischer KW, Barr AH. Partial-volume Bayesian classification of material mixtures in MR volume data using voxel histograms. IEEE Trans Med. Imag. 1998; 17(1): 74-86.

[25] Santago P, Gage HD. Quantification of MR brain images by mixture density and partial volume modeling. IEEE Trans Med. Imag. 1993; 12(3): 566-74.

[26] Suzuki H, Toriwaki J. Automatic segmentation of head MRI images by knowledge guided thresholding. Computerized Medical Imaging and Graphics 1991; 15(4): 233-40.

[27] Joliot M, Mazoyer BM. Three-dimensional segmentation and interpolation of magnetic resonance brain images. IEEE Trans. Med. Imag. 1993; 12(2): 269-77.

[28] Lim KO, Pfefferbaum A. Segmentation of MR brain images into cerebrospinal fluid spaces, white and gray matter. Journal of Computational Assistant Tomography 1989; 13(4):588–93.

[29] Kundu A. Local segmentation of biomedical images. Computerized Medical Imaging and Graphics 1990; 14:173–83.

[30] Held K, Kops ER, Krause BJ, Wells WM, Kikinis R, Muller-Gartner HW. Markov random field segmentation of brain MR images. IEEE Trans. Med. Imag. 1997; 16(6):878-86.

[31] Leemput KV, Maes F, Vandermeulen D, Suetens P. Automated model-based bias field correction of MR images of the brain. IEEE Trans. Med. Imag. 1999; 18: 885-96.

[32] Leemput KV, Maes F, Vandermeulen D, Suetens P. Automated model-based tissue classification of MR images of the brain. IEEE Trans. Med. Imag. 1999; 18: 897-908.

[33] Rajapakse JC, Giedd JN, Rapoport JL. Statistical approach to segmentation of single-channel cerebral MR images. IEEE Trans. Med. Imag. 1997; 16(2):176-86.

[34] Desco M, Gispert JD, Reig S, *et al*. Statistical segmentation of multidimensional brain datasets. Proceedings of SPIE 2001; 4322: 184-93.

[35] Bezdek JC. Pattern Recognition with Fuzzy Objective Function Algorithms. Plenum Press, New York, 1981.

[36] Liew AWC, Leung SH, Lau WH. Segmentation of Color Lip Images by Spatial Fuzzy Clustering. IEEE Trans. Fuzzy System 2003; 11(4): 542-9.

[37] Liew AWC, Yan H, Law NF. Image Segmentation Based on Adaptive Cluster Prototype Estimation. To appear in IEEE Transactions on Fuzzy System.

[38] Liew AWC, Leung SH, Lau WH. Fuzzy Image Clustering Incorporating Spatial Continuity. IEE Proceedings-Vision, Image and Signal Processing 2000; 147(2): 185-92.

[39] Szeto LK, Liew AWC, Yan H, Tang SS. Gene Expression data clustering and visualization based on a binary hierarchical clustering framework. Special issue on "Biomedical Visualization for Bioinformatics", Journal of Visual Languages and Computing 2003; 14: 341-62.

[40] Wu S, Liew AWC, Yan H. Cluster Analysis of Gene Expression Data Based on Self-Splitting and Merging Competitive Learning. IEEE Trans. on Information Technology in Biomedicine 2004; 8(1): 5-15.

[41] Singh M, Patel P, Khosla D, Kim T. Segmentation of functional MRI by K-means clustering. IEEE Trans. Nucl. Sci. 1996; 43: 2030-6.

[42] Gerig G, Martin J, Kikinis R, Kubler O, Shenton M, Jolesz FA. Unsupervised tissue type segmentation of 3D dual-echo MR head data. Image and Vision Computing 1992; 10:346–60.

[43] Hall LO, Bensaid AM, Clarke LP, Velthuizen RP, Silbiger MS, Bezdek JC. A comparison of neural network and fuzzy clustering techniques in segmenting magnetic resonance images of the brain. IEEE Trans. Neural Networks 1992; 3: 672-82.

[44] Brandt ME, Bohan TP, Kramer LA, Fletcher JM. Estimation of CSF, white and gray matter volumes in hydrocephalic children using fuzzy clustering of MR images. Computerized Medical Imaging and Graphics 1994; 18:25-34.

[45] Pham DL, Prince JL. Adaptive fuzzy segmentation of magnetic resonance images. IEEE Trans. Med. Imag. 1999; 18: 737-51.

[46] Liew AWC, Yan H. An Adaptive Spatial Fuzzy Clustering Algorithm for MR Image Segmentation. IEEE Trans. Med. Imag. 2003; 22(9): 1063-75.

[47] Chang YL, Li X. Adaptive Image Region-Growing. IEEE Trans. on Image Processing 1994; 3(6): 868-72.

[48] Adams R, Bischof L. Seeded Region Growing. IEEE Trans. Pattern Anal. Machine Intell. 1994; 16(6): 641-7.

[49] Heinonen T, Dastidar P, Eskola H, Frey H, Ryymin P, Laasonen E. Applicability of semi-automatic segmentation for volumetric analysis of brain lesions. Journal of Medical Engineering & Technology 1998; 22: 173–8.

[50] Tamez-Pena JG, Totterman S, Parker K. Unsupervised statistical segmentation of multispectral volumetric MR images. Proceedings of SPIE, (Medical Imaging 1999), San Diego; 3661: 300-11.

[51] Pohle R, Toennies KD. Segmentation of medical images using adaptive region growing. Proceedings of SPIE (Medical Imaging 2001), San Diego; 4322: 1337-46.

[52] Manousakas IN, Undrill PE, Cameron GG, Redpath TW. Split-and-Merge Segmentation of Magnetic Resonance Medical Images: Performance Evaluation and Extension to Three Dimensions. Computers and Biomedical Research 1998; 31(6): 393–412.

[53] Sijbers J, Scheunders P, Verhoye M, Van der Linden A, Van Dyck D, Raman E. Watershed-based segmentation of 3D MR data for volume quantization. Journal of Magnetic Resonance Imaging 1997; 15: 679-88.

[54] Bueno G, Musse O, Heitz F, Armspach JP. 3D Watershed-based segmentation of internal structures within MR brain images. Medical Images 2000: Image processing, Proc. SPIE, 2000; 3979: 284-93.

[55] Bomans M, Hohne KH, Tiede U, Riemer M. 3D segmentation of MR images of the head for 3D display. IEEE Trans. Med. Imag. 1990; 9(2):177–83.

[56] Ashtari M, Zito JL, Gold BI, Lieberman JA, Borenstein MT, Herman PG. Computerized volume measurement of brain structure. Investigations on Radiolology 1990; 25:798–805.

[57] Dellepiane S. Image segmentation: Errors, sensitivity and uncertainty. Proceedings of the 13th IEEE-Engineering of Medical Biological Society 1994; 13:253–4.

[58] Ji L, Yan H. An attractable snakes based on the greedy algorithm for contour extraction. Pattern Recognition 2002; 35(4):791-806.

[59] McInerney T, Terzopoulos D. Deformable models in medical image analysis: A survey. Medical Image Analysis 1996; 1(2):91-108.

[60] Atkins MS, Mackiewich BT. Fully automatic segmentation of the brain in MRI. IEEE Trans. Med. Imag. 1998; 17: 98–107.

[61] Davatzikos CA, Prince JL. An active contour model for mapping the cortex. IEEE Trans. Med. Imag. 1995; 14 (1): 65–80.

[62] Duta N, Sonka M. Segmentation and interpretation of MR brain images: An improved active shape model. IEEE Trans. Med. Imag. 1998; 17(6):1049-62.

[63] Weerasinghe C, Ji L, Yan H. A new method for ROI extraction from motion affected MR images based on suppression of artifacts in the image background. Signal Processing 2000; 80(5):867-81.

[64] Dawant BM, Hartmann SL, Thirion JP, Maes F, Vandermeulen D, Demaerel P. Automatic 3-D segmentation of internal structures of the head in MR images using a combination of similarity and free-form transformations. I. Methodology and validation on normal subjects. IEEE Trans. Med. Imag. 1999; 18(10): 909-16.

[65] Collins DL, Holmes CJ, Peters TM, Evans AC. Automatic 3D model-based neuroanatomical segmentation. Human Brain Mapping 1995; 3:190-208.

[66] Aboutanos GB, Dawant BM. Automatic brain segmentation and validation: image-based versus atlas-based deformable models. SPIE Proc. Med. Imag. 1997; 3034:299-310.

[67] Arata LK, Dhawan AP, Broderick JP, Gaskil-Shipley MF, Levy AV, Volkow ND. Three-dimensional anatomical model-based segmentation of MR brain images through principal axes registration. IEEE Trans Biomed. Eng. 1995; 42(11):1069-78.

[68] Thompson P, Toga AW. Detection, visualization and animation of abnormal anatomic structure with a probabilistic brain atlas based on random vector field transformations. Med. Image Anal. 1997; 1:271-94.

[69] Gelenbe E, Feng Y, Krishnan KRR. Neural network methods for volumetric magnetic resonance imaging of the human brain. Proc IEEE 1996; 84:1488-96.

[70] Reddick WE, Glass JO, Cook EN, Elkin TD, Deaton RJ. Automated segmentation and classification of multispectral magnetic resonance images of brain using artificial neural networks. IEEE Trans. Med. Imag. 1997; 16:911-8.

[71] Alirezaie J, Jernigan ME. MR image segmentation and analysis based on neural networks. In Signal Processing for Magnetic Resonance Imaging and Spectroscopy, H. Yan Ed., Marcel Dekker, Inc., 2002; 341-64.

[72] Zhu Y. Yan H. Computerized tumor boundary detection using a Hopfield network. IEEE Trans. Med. Imag. 1997; 16(1):55-67.

[73] Available online: http://www.bic.mni.mcgill.ca/brainweb, McGill University, Quebec, ON, Canada.

[74] Cocosco CA, Kollokian V, Kwan RKS, Evans AC. BrainWeb: Online interface to a 3D MRI simulated brain database.

NeuroImage 5(4): part 2/4, S425, Proc. 3rd Int. Conf. on Functional Mapping of the Human Brain, Copenhagen, May 1997.

[75] Collins DL, Zijdenbos AP, Kollokian V, Sled JG, Kabani NJ, Holmes CJ, Evans AC. Design and construction of a realistic digital brain phantom. IEEE Trans. Med. Imag. 1998; 17: 463-8.

[76] Kwan RKS, Evans AC, Pike GB. An extensible MRI simulator for post-processing evaluation. In *Visualization in Biomedical Computing* (VBC'96). Lecture Notes in Computer Science, Springer-Verlag, 1996; 1131: 135-40.

[77] Duncan JS, Ayache N. Medical Image Analysis: Progress over Two Decades and the Challenges Ahead. IEEE Trans. Pattern Anal. Machine Intell. 2000; 22(1): 85-106.